

# Topological synthesis of fluidic pressure-actuated robust compliant mechanisms

**Prabhat Kumar**

Department of Mechanical Engineering  
Indian Institute of Science, Bengaluru 560012, Karnataka, India  
prabhatk@iisc.ac.in

**Matthijs Langelaar**

Department of Precision and Microsystems Engineering  
Delft University of Technology  
2628CD Delft, The Netherlands  
m.langelaar@tudelft.nl

---

## ABSTRACT

This paper presents a density-based topology optimization approach for synthesizing pressure-actuated robust compliant mechanisms. To ensure functionality under manufacturing inaccuracies, the robust or three-field formulation is employed, involving dilated, intermediate and eroded realizations of the design. Darcy's law in conjunction with a conceptualized drainage term is used to model the pressure load as a function of the design vector. The consistent nodal loads are evaluated from the obtained pressure field using the standard finite element method. The objective and load sensitivities are obtained using the adjoint-variable approach. A multi-criteria objective involving both the stiffness and flexibility of the mechanism is employed in the robust formulation, and min-max optimization problems are solved to obtain pressure-actuated inverter and gripper compliant mechanisms with different minimum feature sizes. Limitations of the linear elasticity assumptions while designing mechanisms are identified with high pressure loads.

**Keywords:** Compliant mechanism synthesis, design-dependent pressure loads, robust formulation, geometric nonlinearity, follower forces

---

## 1 Introduction

Compliant mechanisms (CMs) are established concepts in industry and academia offering various advantages over traditional linkage-based counterparts, e.g., less wear and tear, low manufacturing and assembly cost, repeatability and high precision, lack of frictional losses, to name a few. Due to such promising advantages, their usage is continuously rising in a wide variety of applications [1–5]. These mechanisms characterized via monolithic designs are termed CMs, since their functionality arises from the elastic deformations of their flexible (compliant) members in response to the input forces. Finding the optimum balance between output deformation and stiffness when designing CMs is a nontrivial task. Topology optimization (TO) has been shown to be an effective approach for designing such mechanisms [6]. TO is a computational design technique able to achieve the optimized material distribution within a given design domain by extremizing the conceptualized (desired) objectives under a known set of physical and geometrical constraints [7]. In a general structural setting, the design domain is parameterized using finite elements (FEs). Each FE is assigned a material density design variable  $\rho_i \in [0, 1]$ . Here,  $\rho_i = 1$  and

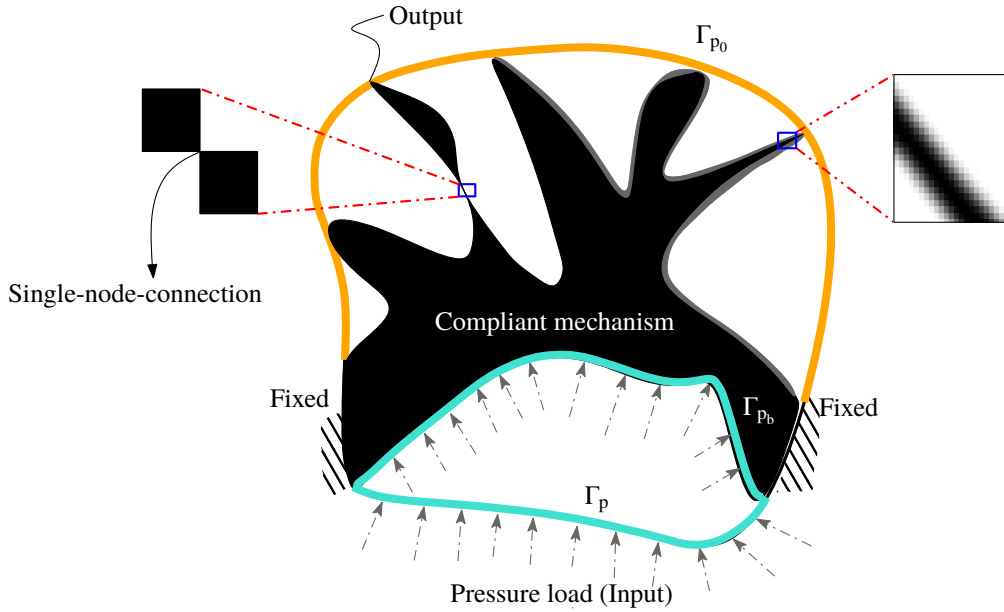


Fig. 1: Schematic diagram of a pressure-actuated compliant mechanism.  $\Gamma_{p_0}$  and  $\Gamma_p$  are the boundaries with zero and finite pressure loading, respectively.  $\Gamma_{p_b}$  is the final pressure boundary for the optimized CM. A single-node hinge and a region with gray FEs are also depicted.

$\rho_i = 0$  represent solid and void states of the  $i^{\text{th}}$  FE, respectively. Ideally, FEs with  $\rho = 1$  should constitute the optimized CMs.

Actuating forces of CMs can be recognized as either *design-dependent*, e.g., pneumatic, hydraulic pressure loads, or *design-independent*, e.g., constant forces. Design-dependent pressure loads<sup>1</sup> alter their magnitude, location and/or direction as the design boundary on which they act evolves during the TO process. Consequently, such loads pose many challenges for the TO formulation, e.g., locating a valid surface to apply the loads, relating pressure field to the design vector, and evaluating consistent nodal forces and their sensitivities with respect to the design vector [8]. *Pressure-actuated CMs (P-CMs)* constitute a relatively novel category of mechanisms that find application in e.g. pneumatically or hydraulically actuated soft robots (mechanisms) [9, 10]. Note however that, in order to attain maximum flexibility, CMs designed via classical TO are prone to exhibit single-node-connected hinges and gray density FEs ( $0 < \rho < 1$ ) in the optimized designs [11, 12]. Such features cannot be realized, and in order to render the design manufacturable, post-processing of the optimized geometry is necessary which can severely affect the optimized performance. This challenge is found in P-CMs designed by TO as well, where it can be even more detrimental given the close relation between boundary shape and loading. A schematic figure of a P-CM is depicted in Fig. 1 wherein the pressure loading boundary moves from its initial surface  $\Gamma_p$  to the final (optimized) surface  $\Gamma_{p_b}$ . Furthermore, Fig. 1 depicts a single-node hinge and region with gray FEs. Given the negative effect such features have on the manufacturability and performance of P-CMs, it is important to control and avoid them. The need to generate P-CM designs whose actual performance closely matches the simulated optimized performance forms the motivation for the present study.

First we discuss existing approaches in TO of pressure-loaded structures and introduce the method used in this work. Hammer and Olhoff [13] were first to present an approach to design pressure-loaded structures. A fictitious thermal loading setting was exploited to solve pressure-loaded design problems by Chen and Kikuchi [14]. Sigmund and Clausen [15] used the mixed-finite element method [16] with a three-phase material (solid, void, fluid) formulation in their approach. The mixed-finite element approaches require satisfaction of the BB condition for the stability in the FE analysis [16]. Chen et al. [17] employed the approach presented in [14] to design P-CMs. Panganiban et al. [18] used a nonconforming FE method which is not a standard FE method. Vasista and Tong [19]

<sup>1</sup>We henceforth for brevity write pressure loads instead of design-dependent pressure loads.

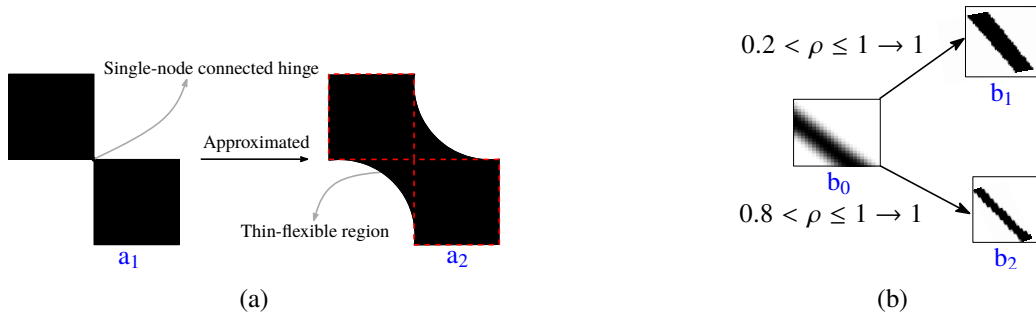


Fig. 2: Schematic diagrams for a single-node connection and design thresholding are depicted in (a) and (b), respectively. (a) shows one of the ways to approximate the design around a single-node connection into a thin-flexible region and therefore, the fabricated mechanisms may have lower performance than the corresponding numerical results. (b) depicts how the different threshold material densities result in different material layouts for manufacturing and thus, performance of the fabricated P-CM depends upon the threshold density one chooses during design extraction.

used the solid isotropic material with penalization (SIMP) and the moving isosurface threshold methods in their approach. de Souza and Silva [20] also employed the method proposed in [15]. In our previous study [8], the authors presented a design method using Darcy's law in conjunction with a drainage term. In that work we also demonstrated the importance of load sensitivities in designing of the P-CMs. The method proposed in [8] uses the standard FE formulation, provides consistent sensitivities and was found to work well in generating P-CMs for two- and three-dimensional as well [21]. Therefore, it will also be used in the present study.

For the design optimization process to be useful and reliable, it is important that as-fabricated P-CMs perform similar to the prediction made by the numerical simulation used in the optimization process. However, with existing methods a significant decline in actual performance can arise compared to the numerical predictions, as noted above. This is primarily due to three factors: (A) inaccurate and/or approximate conversion of one-node-connected hinges to thin-flexible regions (Fig. 2a) and inaccuracies introduced by unrealistic representation of thin, flexible regions in FE models used in TO, (B) CMs being overly sensitive to manufacturing inaccuracies or arbitrariness in design extraction (Fig. 2b), and (C) the use of small displacement analysis and linear elasticity assumptions for the P-CM designs.

Firstly, one-node-connected hinges (Fig. 2a), artificially stiff locations, appear due to deficiencies in the FE analysis with quadrilateral FEs that permit load transfer with zero rotational stiffness [11, 12]. Such hinges pose challenges in accurate design interpretation of the optimized mechanisms, since real compliant hinges will always have a finite rotational stiffness [11, 12]. One of the methods for approximating a one-node-connected location for fabrication may be as depicted in Fig. 2a, which results in a thin-flexible region and thus, the performance of the numerical design (Fig. 2a- $a_1$ ) will differ from that of the fabricated one (Fig. 2a- $a_2$ ). Various ways have been proposed to prevent formation of single-node-connected hinges in CMs [12, 22–24], but these have not yet been applied to and evaluated for P-CM TO. Secondly, in a standard density-based TO setting with a gradient-based optimizer, it is difficult to obtain pure 0-1 solutions (Fig. 1). Therefore, extraction of the optimized designs based on the considered density threshold (Fig. 2b) is required, which invariably alters the final designs and thus, the performances with respect to the numerical predictions. Fig. 2b illustrates a scenario to indicate how the different threshold material densities lead to different material (contour) layouts (Fig. 2b- $b_1$  and Fig. 2b- $b_2$ ) and thus, the corresponding fabricated P-CM and potentially also its loading (significantly) differs from that obtained via TO.

Thirdly, a typical P-CM or CM may experience large deflection and also, contact between branches, i.e., self-contact [25, 27] and external/mutual contact [26, 27] thus, TO design approaches must include nonlinear mechanics (with contact formulation) to predict mechanism performance [26, 27]. However, nonlinear structural analysis poses various challenges in TO [4, 28], which can even get more pronounced in combination with pressure loads whose magnitude, direction and/or location vary and follow the surfaces/facets where they are applied. To model the characteristics of pressure loads, one needs to include the follower force concepts in the design approach, which demands a dedicated and in-depth investigation within a TO setting, which is out of the scope of this paper.

Therefore, instead of addressing this point at the TO stage, we choose to investigate and assess its influence based on the P-CM designs generated using linear modeling.

To address the outlined challenges, in this study we take the following approaches:

1. The robust or three-field formulation [24] is adopted to address problems A and B, by its ability to impose a minimum length scale and to reduce the sensitivity of the final design to post-processing or manufacturing errors.
2. Nonlinear FEA is used to analyze optimized P-CM designs with a neo-Hookean hyperelastic material model and increased pressure loads to investigate the large deformation behavior and to determine the limitations of the linear elastic assumptions.

While the robust formulation [24] is expected to solve factors A and B given results reported in literature [24], this has as of yet not been investigated or confirmed for P-CM, which is the specific interest of this study. Next to this, the nonlinear FEA study is not intended as a solution to the lack of large-displacement analysis during P-CM TO, but our aim is to provide a quantitative assessment of the severity of the error introduced by this simplification, in representative design cases. In addition, nonlinear finite element analyses are used to assess the sensitivity of standard and robust P-CMs to design extraction choices/ manufacturing errors. Due to computational limitations and for clarity of presentation this study has been carried out in a 2D setting. Its findings nonetheless are expected to apply to general 3D cases as well.

This paper is organized as follows. Sec. 2 presents modeling of the pressure loads as a function of the design vector using the Darcy law with a drainage term, in line with [8]. Using a transformation matrix, the consistent nodal loads are evaluated. The TO formulation with the robust approach together with the corresponding sensitivity analysis is described in Sec. 3. Next, in Sec. 4 numerical examples of designing robust pressure-actuated inverter and gripper mechanisms are presented. The optimized P-CM designs are extracted, and nonlinear FE analyses are performed in ABAQUS with high pressure loads to investigate large deformation behavior of the CMs. Lastly, conclusions are drawn in Sec. 5.

## 2 Design-dependent pressure load modeling and consistent nodal forces

In this section, modeling of the pressure field as a function of the design variables, finite element formulation and consistent nodal loads evaluation are summarized. For a detailed description, we refer to our previous paper [8].

As per the Darcy law, one evaluates flux  $\mathbf{q}$  in terms of the pressure gradient  $\nabla p$ , the permeability  $\kappa$  of the medium and the fluid viscosity  $\mu$  as

$$\mathbf{q} = -\frac{\kappa}{\mu} \nabla p = -K(\bar{\rho}) \nabla p, \quad (1)$$

where  $\bar{\rho}$  and  $K(\bar{\rho})$  represent the physical density (see Sec. 3) and the flow coefficient of an FE, respectively. In a typical density-based TO setting, an FE displays two states, therefore the actual flow coefficient  $K(\bar{\rho}_e)$  of an FE is determined using the flow coefficients associated to its solid and void phases interpolated by a smooth Heaviside projection function  $\mathcal{H}(\bar{\rho}_e, \beta_\kappa, \eta_\kappa)$  as

$$K(\bar{\rho}_e) = K_v (1 - (1 - \epsilon) \mathcal{H}(\bar{\rho}_e, \beta_\kappa, \eta_\kappa)), \quad (2)$$

where  $\mathcal{H}(\bar{\rho}_e, \beta_\kappa, \eta_\kappa) = \frac{\tanh(\beta_\kappa \eta_\kappa) + \tanh(\beta_\kappa (\bar{\rho}_e - \eta_\kappa))}{\tanh(\beta_\kappa \eta_\kappa) + \tanh(\beta_\kappa (1 - \eta_\kappa))}$ , and  $\epsilon = \frac{K_s}{K_v}$  is the flow contrast [21].  $K_s$  and  $K_v$  indicate the flow coefficients of the solid and void states, respectively. Further,  $\eta_\kappa$  and  $\beta_\kappa$  control the step position and the slope of  $K(\bar{\rho}_e)$ , respectively. In addition, a drainage term  $Q_{\text{drain}}$  conceptualized in [8] and numerically qualified in [21] is employed that helps achieve a localized pressure gradient at solid-void interfaces. It is defined in terms of a drainage coefficient  $D(\bar{\rho}_e)$ , instantaneous pressure field  $p$  and output pressure  $p_{\text{ext}}$  as

$$Q_{\text{drain}} = -D(\bar{\rho}_e)(p - p_{\text{ext}}), \quad (3)$$

where the drainage coefficient  $D(\bar{\rho}_e) = D_s \mathcal{H}(\bar{\rho}_e, \beta_d, \eta_d)$ .  $\beta_d$  and  $\eta_d$  are two parameters that control the values of  $D(\bar{\rho}_e)$ .  $D_s$  is the drainage coefficient of a solid FE, which is equal to [8]

$$D_s = \left( \frac{\ln r}{\Delta s} \right)^2 K_s, \quad (4)$$

where  $r$  is the ratio of input pressure at depth  $\Delta s$ , i.e.,  $p|_{\Delta s} = r p_{\text{in}}$  and the penetration depth  $\Delta s$  can be set equal to the width or height of a few FEs. Using  $Q_{\text{drain}}$ , Eq. 1 transpires per [8] as

$$\nabla \cdot \mathbf{q} - Q_{\text{drain}} = 0. \quad (5)$$

In a discrete FE setting, one writes the weak form of Eq. 5 for an FE with domain  $\Omega_e$  as [8]

$$\underbrace{\int_{\Omega_e} \left( K \mathbf{B}_p^\top \mathbf{B}_p + D \mathbf{N}_p^\top \mathbf{N}_p \right) d\Omega_e}_{\mathbf{A}_e} \mathbf{p}_e = \underbrace{\int_{\Omega_e} D \mathbf{N}_p^\top p_{\text{ext}} d\Omega_e - \int_{\Gamma_e} \mathbf{N}_p^\top \mathbf{q}_\Gamma \cdot \mathbf{n}_e d\Gamma_e}_{\mathbf{f}_e}, \quad (6)$$

where  $\mathbf{p}_e$  is the pressure field to be evaluated,  $\mathbf{B}_p = \nabla \mathbf{N}_p$  with  $\mathbf{N}_p = [N_1, N_2, N_3, N_4]$  are the bi-linear shape functions for a quadrilateral FE.  $\mathbf{A}\mathbf{p} = \mathbf{f}$  is the global form of Eq. 6 with  $\mathbf{p}$  is the global pressure load vector. In this work,  $p_{\text{ext}}$  and  $\mathbf{q}_\Gamma$  are set to zero, therefore  $\mathbf{f} = \mathbf{0}$ , i.e.,  $\mathbf{A}\mathbf{p} = \mathbf{0}$ . Using the obtained global pressure field  $\mathbf{p}$ , the consistent global nodal forces  $\mathbf{F} = -\mathbf{T}\mathbf{p}$  are determined using a transformation matrix  $\mathbf{T}$  whose elemental form  $\mathbf{T}_e$  is related to that of nodal force  $\mathbf{F}_e$  as [8]

$$\mathbf{F}^e = \mathbf{T}_e \mathbf{p}_e = - \int_{\Omega_e} \mathbf{N}_u^\top \mathbf{B}_p d\Omega_e \mathbf{p}_e, \quad (7)$$

where  $\mathbf{N}_u = [N_1 \mathbf{I}, N_2 \mathbf{I}, N_3 \mathbf{I}, N_4 \mathbf{I}]$  with  $\mathbf{I}$  the identity matrix in  $\mathcal{R}^2$ . In summary, one employs Eq. 6 for determining the pressure field, whereas the corresponding consistent nodal force vector for an FE is evaluated using Eq. 7. Note that through the use of smooth Heaviside functions the loads are a differentiable function of the density variables. This allows performing load sensitivity analysis readily, as detailed in [8] and further elaborated in Sec. 3.2.

### 3 Robust P-CM topology optimization formulation

The three-field  $(\rho, \tilde{\rho}, \bar{\rho})$  representation of the design domain is considered [29]. The filtered design variable  $\tilde{\rho}_j$  of element  $j$  is determined using weighted average of the design variables  $\rho$  pertaining to neighboring FEs lying within a circular region of radius  $r_{\text{fill}}$  [30]. Mathematically,

$$\tilde{\rho}_j = \frac{\sum_{k=1}^{N_e} v_k \rho_k w(\mathbf{x}_k)}{\sum_{k=1}^{N_e} v_k w(\mathbf{x}_k)} \quad (8)$$

where  $N_e$  is the total number of neighboring elements of the  $j^{\text{th}}$  FE, and  $v_k$  is the volume of neighboring element  $k$ . The weight function  $w(\mathbf{x}_k) = \max\left(0, 1 - \frac{d}{r_{\text{fill}}}\right)$ , wherein  $d = \|\mathbf{x}_j - \mathbf{x}_k\|$  is a Euclidean distance between centroids  $\mathbf{x}_j$  and  $\mathbf{x}_k$  of elements  $j$  and  $k$ , respectively.  $r_{\text{fill}}$  is called filter radius for the considered design problems. The

derivative of  $\tilde{\rho}_j$  (Eq. 8) with respect to  $\rho_k$  is

$$\frac{\partial \tilde{\rho}_j}{\partial \rho_k} = \frac{v_k w(\mathbf{x}_k)}{\sum_{i=1}^{N_e} v_i w(\mathbf{x}_i)}. \quad (9)$$

The physical design variable  $\bar{\rho}_j$  is defined as [24]

$$\bar{\rho}_j(\tilde{\rho}_j, \beta, \eta) = \frac{\tanh(\beta\eta) + \tanh(\beta(\tilde{\rho}_j - \eta))}{\tanh(\beta\eta) + \tanh(\beta(1 - \eta))}, \quad (10)$$

where  $\beta \in [0, \infty)$  and  $\eta \in [0, 1]$  control the steepness and the threshold of the projection function, respectively. To achieve the optimized solutions close to black and white designs, typically  $\beta$  is increased from an initial value  $\beta_{\text{int}} = 1$  to a maximum value  $\beta_{\text{max}}$  using a continuation strategy.  $\eta = 0$  ensures the minimum length scale on the solid phase [24], whereas that of solid phase is obtained using  $\eta = 1$ . Note that when using  $\eta = 0$  and  $\eta = 1$ , Eq. 10 yields the Heaviside step approximation function given in [31] and the modified Heaviside step approximation function mentioned in [32], respectively. The derivative of  $\bar{\rho}_j$  with respect to  $\tilde{\rho}_j$  is

$$\frac{\partial \bar{\rho}_j}{\partial \tilde{\rho}_j} = \beta \frac{1 - \tanh(\beta(\tilde{\rho}_j - \eta))^2}{\tanh(\beta\eta) + \tanh(\beta(1 - \eta))}. \quad (11)$$

Having noted the derivatives in Eqs. 9 and 11, the chain rule is used to determine the derivatives of a function  $f$  with respect to  $\rho_k$  as

$$\frac{\partial f}{\partial \rho_k} = \sum_{j=1}^{N_e} \frac{\partial f}{\partial \bar{\rho}_j} \frac{\partial \bar{\rho}_j}{\partial \tilde{\rho}_j} \frac{\partial \tilde{\rho}_j}{\partial \rho_k}, \quad (12)$$

where  $\frac{\partial f}{\partial \bar{\rho}_j}$  is evaluated using the adjoint-variable method (see Sec. 3.2). We use the modified SIMP (Simplified Isotropic Material with Penalization) method to interpolate the Young's modulus of each FE using its physical design variable  $\bar{\rho}_j$  as

$$E_1(\bar{\rho}_j) = E_0 + (\bar{\rho}_j)^\zeta (E_1 - E_0), \quad \bar{\rho}_j \in [0, 1] \quad (13)$$

where  $E_1$  and  $E_0$  are Young's moduli of the solid and void phases of an FE, respectively. The material contrast, i.e.,  $\frac{E_0}{E_1} = 10^{-6}$  is set, and the penalty factor  $\zeta = 3$  is used in order to steer the topology optimization towards a '0-1' solution.

### 3.1 Robust formulation

The robust formulation is employed wherein three physical density fields, i.e., dilated  $\bar{\rho}^d$ , intermediate (blueprint)  $\bar{\rho}^i$  and eroded  $\bar{\rho}^e$ , are considered for the design domain [24]. Erosion and dilation are morphological image operators, which can be used in TO for e.g. robustness and feature size control [32]. Assuming uniform manufacturing errors, maximum and minimum manufacturing limits are indicated by the dilated and eroded designs respectively, whereas the intermediate (blueprint) ones denote the desired manufacturing limit. Here,  $0.5 + \Delta\eta$ ,  $0.5$  and  $0.5 - \Delta\eta$  in Eq. 10 are used in place of  $\eta$  to evaluate  $\bar{\rho}^e$ ,  $\bar{\rho}^i$  and  $\bar{\rho}^d$ , respectively. The deviation  $\Delta\eta \in [0, 0.5]$  is a user defined parameter, which in combination with the filter radius  $r_{\text{fil}}$  determines the minimum length scale on the solid and void phases [33].

The optimization problem is formulated as a min-max problem [24]

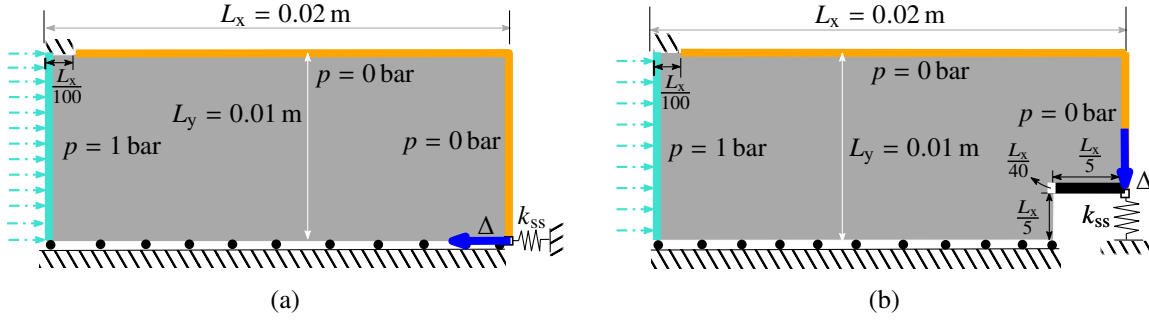


Fig. 3: Symmetric half design domains of the mechanisms. (a) Inverter design domain and (b) Gripper design domain. The dimensions of the design domains are  $L_x = 0.02$  m and  $L_y = 0.01$  m, where  $L_x$  and  $L_y$  indicate dimensions in  $x$ - and  $y$ -directions, respectively. In both mechanisms, the input pressure load is applied on the left edge, and zero pressure is applied at the other edges except the symmetric boundary. Symmetric boundaries and fixed boundaries are also depicted. Workpiece stiffnesses are represented via the output springs with stiffnesses  $k_{ss}$ . In gripper mechanism domain, a non-design void region having area  $\frac{L_x}{5} \times \frac{L_x}{5}$  and a solid region having area  $\frac{L_x}{5} \times \frac{L_x}{40}$  are used at the right lower part.

$$\begin{array}{l}
 \min_{\rho} : \max : \left( f_0(\bar{\rho}^d(\rho)), f_0(\bar{\rho}^i(\rho)), f_0(\bar{\rho}^e(\rho)) \right) \\
 s.t. : \mathbf{A}(\rho^l)\mathbf{p}(\rho^l) = \mathbf{0}, \quad l = d, i, e \\
 \quad \mathbf{K}(\rho^l)\mathbf{u}(\rho^l) = \mathbf{F} = -\mathbf{D}\mathbf{p}(\rho^l) \\
 \quad \mathbf{K}(\rho^l)\mathbf{v}(\rho^l) = \mathbf{F}_d \\
 \quad V(\bar{\rho}^d(\rho)) - V_d^* \leq 0 \\
 \quad \mathbf{0} \leq \rho \leq \mathbf{1}
 \end{array} \quad (14)$$

where  $f_0$  is a multi-criteria objective aimed at obtaining effective compliant mechanisms [34] defined by  $-\mu \frac{MSE}{SE}$ , with  $MSE = \mathbf{v}^T \mathbf{K} \mathbf{u}$  and  $SE = \frac{1}{2} \mathbf{u}^T \mathbf{K} \mathbf{u}$ .  $MSE$  and  $SE$  represent the mutual strain energy and strain energy of the mechanism, respectively.  $\mu$  is the scaling factor used to scale the objective for optimizer compatibility. Note that the multi-criteria objective proposed in [1] finds an optimum trade-off between the flexibility and strength of the mechanisms.  $V(\bar{\rho}^d(\rho)) = \sum_{m=1}^{n_e} V_m \bar{\rho}_m^d$ , where  $V_m$  is the volume of  $m^{\text{th}}$  element whose dilated density is  $\bar{\rho}_m^d$ . The volume constraint is imposed using the dilated design wherein the actual volume of the dilated design is updated after a specific number of optimization iterations such that the volume of the intermediate design becomes equal to the permitted one at the end of the optimization when the volume constraint becomes active [24]. Further,  $V_d^* = \frac{V_i^*}{V(\bar{\rho}^i(\rho))} V(\bar{\rho}^d(\rho))$ , where  $V_d^*$  denotes upper limit of the volume fraction of the dilated design,  $V_i^*$  and  $V(\bar{\rho}^i(\rho)) = \sum_{m=1}^{n_e} V_m \bar{\rho}_m^i(\rho)$  are the prescribed and actual volumes of the intermediate design, respectively.

The robust formulation (Eq. 14) requires solutions to three state equations pertaining to  $\mathbf{u}$ ,  $\mathbf{p}$ ,  $\mathbf{v}$  fields and also furnishes three optimized designs with only one design vector  $\rho$ . The discreteness of the optimized solutions is measured using a gray scale indicator  $M_{nd}$  defined as [32]

$$M_{nd} = \frac{\sum_{e=1}^{n_e} 4(\bar{\rho}_e)(1 - \bar{\rho}_e)}{n_e}, \quad (15)$$

where  $n_e$  is the total number of elements employed to discretize the design domain.

### 3.2 Sensitivity analysis

We use the Method of Moving Asymptotes (MMA) [35], a gradient-based optimizer, for solving the optimization problem (Eq. 14). A standard setting available in the MMA optimizer is used to solve the min-max



Parameter	Notation	Value
Young's modulus of actual material	$E_1$	$3 \times 10^9 \text{ N m}^{-2}$
Poisson's ratio	$\nu$	0.40
Out-of-plane thickness	$t$	0.01 m
Penalization	$\zeta$	3
Young's modulus of a void FE ( $\rho = 0$ )	$E_0$	$E_1 \times 10^{-6} \text{ N m}^{-2}$
External move limit	$\Delta \rho$	0.1 per iteration
Input pressure load	$p_{\text{in}}$	$1 \times 10^5 \text{ N m}^{-2}$
$K(\rho)$ step location	$\eta_k$	0.3
$K(\rho)$ slope at step	$\beta_k$	10
$H(\rho)$ step location	$\eta_h$	0.2
$H(\rho)$ slope at step	$\beta_h$	10
Flow coefficient of a void FE	$k_v$	$1 \text{ m}^4 \text{ N}^{-1} \text{ s}^{-1}$
Flow coefficient of a solid FE	$k_s$	$k_v \times 10^{-7} \text{ m}^4 \text{ N}^{-1} \text{ s}^{-1}$
Drainage from solid	$h_s$	$\left(\frac{\ln r}{\Delta s}\right)^2 k_s$
Remainder of input pressure at $\Delta s$	$r$	0.1

Table 1: Various parameters used in this paper.

optimization problem. The Lagrangian  $\mathcal{L}$  using the objective function and constraints can be written as

$$\mathcal{L} = f_0(\bar{\rho}) + \lambda_1^\top (\mathbf{K}\mathbf{u} + \mathbf{H}\mathbf{p}) + \lambda_2^\top (\mathbf{A}\mathbf{p}) + \lambda_3^\top (\mathbf{K}\mathbf{v} - \mathbf{F}_d) + \Lambda \left( V(\bar{\rho}^d(\rho)) - V_d^* \right), \quad (16)$$

where  $\lambda_i|_{i=1,2,3}$  and  $\Lambda$  are the Lagrange multipliers. Using the adjoint equations corresponding to Eq. 16, i.e.,  $\frac{\partial \mathcal{L}}{\partial \mathbf{u}} = 0$ ,  $\frac{\partial \mathcal{L}}{\partial \mathbf{p}} = 0$ , and  $\frac{\partial \mathcal{L}}{\partial \mathbf{v}} = 0$ , one finds the Lagrange multipliers  $\lambda_1$ ,  $\lambda_2$  and  $\lambda_3$  as [8]

$$\left. \begin{aligned} \lambda_1^\top &= -\frac{\partial f_0(\mathbf{u}, \mathbf{v}, \rho)}{\partial \mathbf{u}} \mathbf{K}^{-1} \\ \lambda_2^\top &= -\lambda_1^\top \mathbf{H} \mathbf{A}^{-1} \\ \lambda_3^\top &= -\frac{\partial f_0(\mathbf{u}, \mathbf{v}, \rho)}{\partial \mathbf{v}} \mathbf{K}^{-1} \end{aligned} \right\}. \quad (17)$$

The design equation corresponding to Eq. 16 is

$$\begin{aligned} \frac{\partial \mathcal{L}}{\partial \bar{\rho}} &= \frac{\partial f_0}{\partial \bar{\rho}} + \lambda_1^\top \frac{\partial \mathbf{K}}{\partial \bar{\rho}} \mathbf{u} + \lambda_2^\top \frac{\partial \mathbf{A}}{\partial \bar{\rho}} \mathbf{p} + \lambda_3^\top \frac{\partial \mathbf{K}}{\partial \bar{\rho}} \mathbf{v} + \Lambda \frac{\partial (V(\bar{\rho}^d(\rho)) - V_d^*)}{\partial \bar{\rho}} \\ &= \underbrace{\frac{\partial f_0}{\partial \bar{\rho}} + \lambda_1^\top \frac{\partial \mathbf{K}}{\partial \bar{\rho}} \mathbf{u} + \lambda_2^\top \frac{\partial \mathbf{A}}{\partial \bar{\rho}} \mathbf{p} + \lambda_3^\top \frac{\partial \mathbf{K}}{\partial \bar{\rho}} \mathbf{v}}_{\Theta} + \Lambda \frac{\partial (V(\bar{\rho}^d(\rho)))}{\partial \bar{\rho}}, \end{aligned} \quad (18)$$

with complementarity condition  $\Lambda (V(\bar{\rho}^d(\rho)) - V_d^*) = 0$ ,  $\Lambda \geq 0$ . Using  $f_0 = -\mu \frac{MSE}{SE}$  and in view of Eq. 17,  $\Theta$



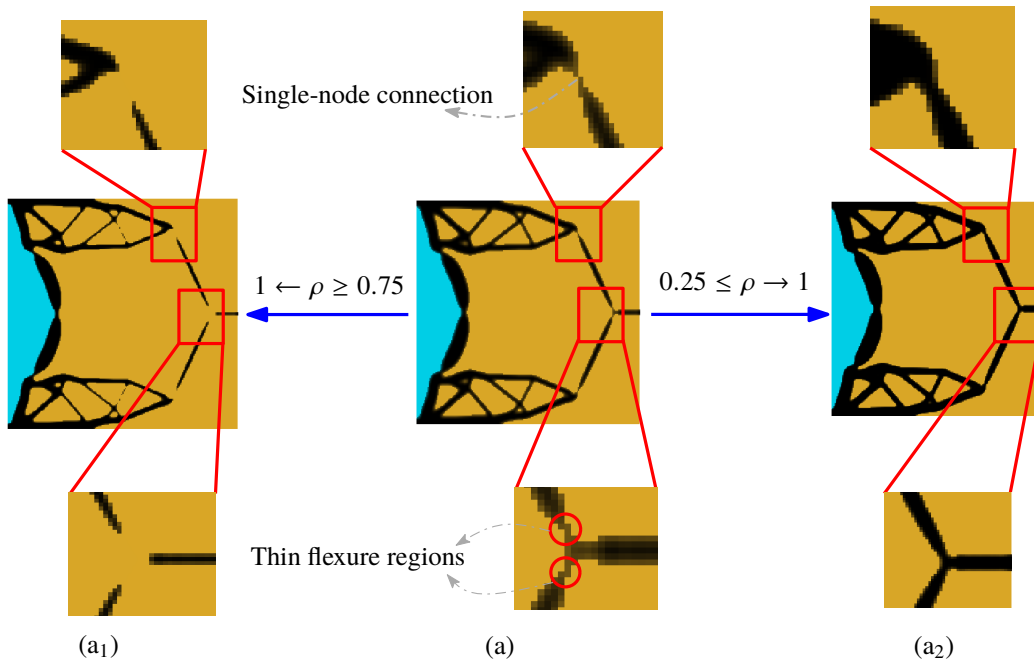


Fig. 4: An optimized pressure-actuated inverter mechanism obtained using the method presented in [8] is displayed in (a). FEs with  $\rho > 0.49$  are used to show the result in (a). The optimized design contains one-node-connected hinges and thin flexure regions surrounded by gray elements that are depicted in insets. Using the two different thresholds, the approximated designs are displayed in (a<sub>1</sub>) and (a<sub>2</sub>).

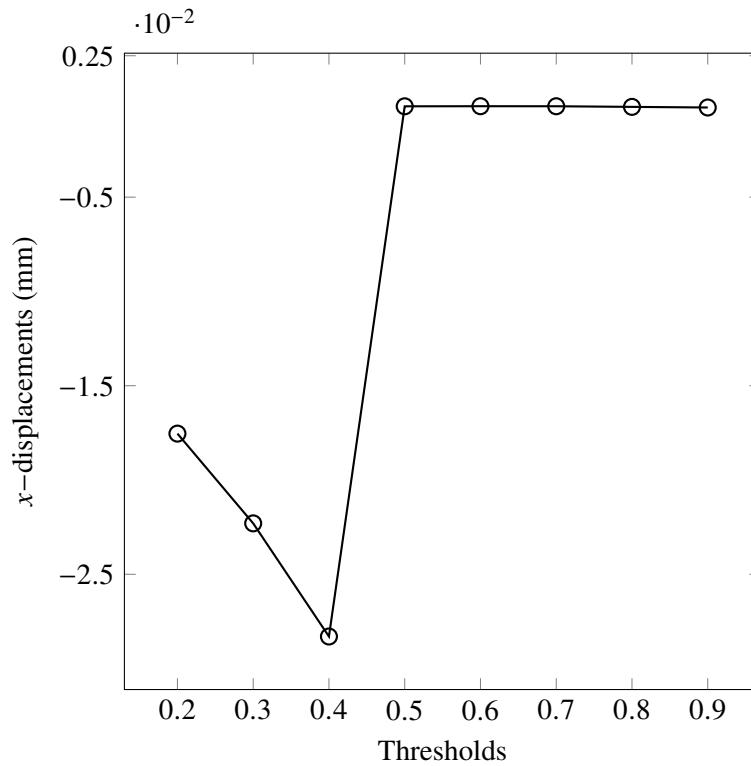


Fig. 5: The output displacements of the traditionally designed pressure-actuated inverter mechanisms at different threshold material densities  $\rho_{th}$ .



(a) Eroded design,  $\Delta = 0.097$  mm  
 $\Delta\eta = 0.15$ :  $M_{nd} = 0.65\%$ ,  $V_f = 0.15$



(b) Intermediate design,  $\Delta = 0.071$  mm  
 $M_{nd} = 0.36\%$ ,  $V_f = 0.20$



(c) Dilated design,  $\Delta = 0.046$  mm  
 $M_{nd} = 0.16\%$ ,  $V_f = 0.243$



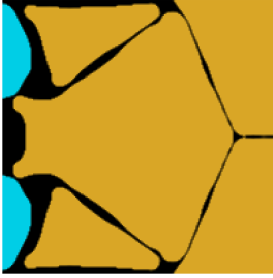
(d) Eroded design,  $\Delta = 0.091$  mm  
 $\Delta\eta = 0.05$ :  $M_{nd} = 0.38\%$ ,  $V_f = 0.186$



(e) Intermediate design,  $\Delta = 0.080$  mm  
 $M_{nd} = 0.58\%$ ,  $V_f = 0.20$



(f) Dilated design,  $\Delta = 0.069$  mm  
 $M_{nd} = 0.11\%$ ,  $V_f = 0.212$



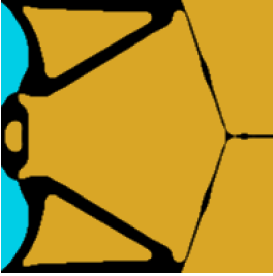
(g) Eroded design,  $\Delta = 0.142$  mm  
 $\Delta\eta = 0.15$ :  $M_{nd} = 1.19\%$ ,  $V_f = 0.13$



(h) Intermediate design,  $\Delta = 0.076$  mm  
 $M_{nd} = 0.59\%$ ,  $V_f = 0.020$



(i) Dilated design,  $\Delta = 0.040$  mm  
 $M_{nd} = 0.43\%$ ,  $V_f = 0.25$



(j) Eroded design,  $\Delta = 0.110$  mm  
 $\Delta\eta = 0.05$ :  $M_{nd} = 0.88\%$ ,  $V_f = 0.175$



(k) Intermediate design,  $\Delta = 0.086$  mm  
 $M_{nd} = 0.81\%$ ,  $V_f = 0.20$



(l) Dilated design,  $\Delta = 0.066$  mm  
 $M_{nd} = 0.42\%$ ,  $V_f = 0.22$

Fig. 6: The robust pressure-actuated inverter mechanisms. Filter radius  $5.4h$  is used for the optimized results shown in rows 1 and 2, whereas for the results displayed in rows 3 and 4, it is set to  $8.4h$ . Note  $h = \min(\frac{L_x}{N_{ex}}, \frac{L_y}{N_{ey}})$ .

transpires as

$$\Theta = \mu \left[ \frac{MSE}{(SE)^2} \left( -\frac{1}{2} \mathbf{u}^\top \frac{\partial \mathbf{K}}{\partial \bar{\rho}} \mathbf{u} \right) + \frac{1}{SE} \left( \mathbf{u}^\top \frac{\partial \mathbf{K}}{\partial \bar{\rho}} \mathbf{v} \right) + \underbrace{\frac{MSE}{(SE)^2} \left( \mathbf{u}^\top \mathbf{H} \mathbf{A}^{-1} \frac{\partial \mathbf{A}}{\partial \bar{\rho}} \mathbf{p} \right) + \frac{1}{SE} \left( -\mathbf{v}^\top \mathbf{H} \mathbf{A}^{-1} \frac{\partial \mathbf{A}}{\partial \bar{\rho}} \mathbf{p} \right)}_{\text{Load sensitivities}} \right]. \quad (19)$$

Now, using Eq. 18 in association with the chain rule given in Eq. 12, one can find the sensitivity of  $\mathcal{L}$  with respect to the design vector, i.e.,  $\frac{d\mathcal{L}}{d\rho}$ . This formulation facilitates straightforward evaluation of the load sensitivities (Eq. 19) that affect the optimized designs of P-CMs [8] and therefore, are important to consider while designing such mechanisms.

#### 4 Numerical examples and discussions

This section evaluates the presented approach by designing pressure-actuated robust inverter and gripper CMs. The symmetric half design domains for designing these mechanisms are displayed in Fig. 3.  $L_x = 0.02$  m and  $L_y = 0.01$  m are set, where  $L_x$  and  $L_y$  represent the dimension in  $x$ - and  $y$ -directions, respectively. 1 bar pressure load is applied on the left edge of the domains, whereas remaining edges excluding the symmetric ones experience zero pressure loading. The fixed parts of the domains and their symmetry boundaries are also depicted. Springs with spring stiffnesses  $k_{ss} = 1 \times 10^4$  N m<sup>-1</sup> represent the workpiece at mechanism output locations (Fig. 3). Table 1 summarizes the design parameters used in the optimization. We use  $N_{ex} \times N_{ey} = 200 \times 100$  bi-linear quadrilateral FEs to parameterize the symmetric half design domains (Fig. 3), where  $N_{ex}$  and  $N_{ey}$  indicate FEs in  $x$ - and  $y$ -directions, respectively. A density-based TO approach with one design variable for each FE is employed with plane stress conditions. The design variable is considered constant within each FE. The external move limit of the MMA optimizer is set to 0.1.

##### 4.1 Traditional pressure-actuated inverter mechanism

The symmetric half design domain displayed in Fig. 3a is considered, and the optimization formulation presented in [8] is employed for designing the inverter mechanism. The filter radius  $r_{fill}$  is set to  $3 \times \max(\frac{L_x}{N_{ex}}, \frac{L_y}{N_{ey}})$ . 20% material volume is permitted. The maximum number of the optimization iterations is fixed to 200.

Fig. 4a depicts the optimized inverter mechanism with final pressure field.  $M_{nd} = 13.43\%$  and  $\Delta = 0.072$  mm are found. Insets in Fig. 4a display the localized single-node-connected hinges and thin flexure regions constituted via gray elements. These geometrical anomalies pose challenges in manufacturing and thus, they are undesirable. When the optimized design is approximated using: (i)  $\rho \in [0.75, 1] \rightarrow 1$  and  $\rho \in [0, 0.75] \rightarrow 0$  as shown in Fig. 4a<sub>1</sub>, a non-realizable design is obtained with  $\Delta = 5.48 \times 10^{-4}$  mm and (ii)  $\rho \in [0.25, 1] \rightarrow 1$  and  $\rho \in [0, 0.25] \rightarrow 0$  as displayed in Fig. 4a<sub>2</sub>, though a realizable design is found,  $\Delta = 0.026$  mm is obtained that is approximately three times lower than that obtained for the actual design (Fig. 4a). Figure 5 displays the output displacements of the inverter mechanism at different threshold densities  $\rho_{th}$ . It can be noted that when  $\rho_{th} > 0.5$ , the corresponding output displacements are negligible as the output port gets disconnected from the input port (Fig. 4a<sub>1</sub>). Therefore, to circumvent these issues and also, to obtain the optimized solutions close to 0-1 such that contours of the designs can be extracted without performing any approximation for fabrication purpose, as mentioned before, the robust formulation is employed [24].

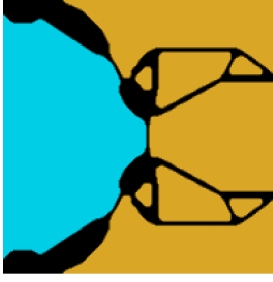
##### 4.2 Robust compliant mechanisms

The various optimized designs of the pressure-actuated inverter and gripper CMs are presented using the robust formulation (Eq. 14). In each case, we get three optimized designs, i.e., the dilated, intermediate and eroded continua, and in those, the intermediate designs are intended for fabrication.

The permitted volume fraction for the intermediate design is set to 0.20 for all the cases. The maximum number of MMA iterations is fixed to 400. In the projection filter (Eq. 10),  $\beta$  is altered from 1 to 128 using a continuation scheme wherein  $\beta$  is doubled after each 50 MMA iteration and once it reaches to 128, it remains so for the remaining optimization iterations. The volume update for the dilated design is performed at each 25<sup>th</sup> MMA iteration.

In case of the inverter CMs, it is desired that the mechanisms provide deformation in the opposite direction of the pressure loading direction, whereas gripping motions are desired in response to the pressure load for the gripper CMs. At the output location of the gripper mechanism, a void area of size  $\frac{L_x}{5} \times \frac{L_x}{5}$  and a solid region of area  $\frac{L_x}{5} \times \frac{L_x}{40}$  are considered to facilitate gripping of a workpiece. We solve the problems using different filter radii and  $\Delta\eta$ .

The full final inverter and gripper mechanisms are obtained by suitably transforming the symmetric half optimized results, and they are depicted in Fig. 6 and Fig. 7, respectively. Note the absence of one-node hinges–



(a) Eroded design,  $\Delta = 0.095$  mm  
 $\Delta\eta = 0.15$ :  $M_{nd} = 0.26\%$ ,  $V_f = 0.166$



(b) Intermediate design,  $\Delta = 0.074$  mm  
 $M_{nd} = 0.22\%$ ,  $V_f = 0.20$



(c) Dilated design,  $\Delta = 0.052$  mm  
 $M_{nd} = 0.11\%$ ,  $V_f = 0.234$



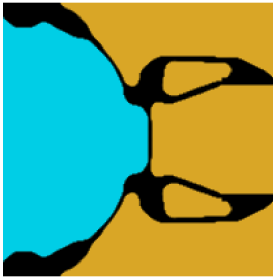
(d) Eroded design,  $\Delta = 0.084$  mm  
 $\Delta\eta = 0.05$ :  $M_{nd} = 0.23\%$ ,  $V_f = 0.19$



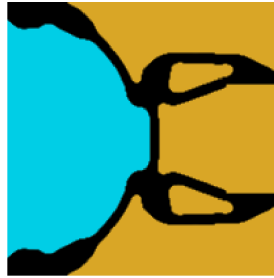
(e) Intermediate design,  $\Delta = 0.068$  mm  
 $M_{nd} = 0.38\%$ ,  $V_f = 0.20$



(f) Dilated design,  $\Delta = 0.062$  mm  
 $M_{nd} = 0.21\%$ ,  $V_f = 0.21$



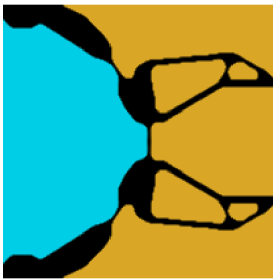
(g) Eroded design,  $\Delta = 0.108$  mm  
 $\Delta\eta = 0.15$ :  $M_{nd} = 0.45\%$ ,  $V_f = 0.15$



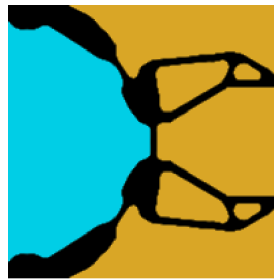
(h) Intermediate design,  $\Delta = 0.064$  mm  
 $M_{nd} = 0.36\%$ ,  $V_f = 0.20$



(i) Dilated design,  $\Delta = 0.039$  mm  
 $M_{nd} = 0.33\%$ ,  $V_f = 0.24$



(j) Eroded design,  $\Delta = 0.087$  mm  
 $\Delta\eta = 0.05$ :  $M_{nd} = 0.68\%$ ,  $V_f = 0.18$



(k) Intermediate design,  $\Delta = 0.068$  mm  
 $M_{nd} = 0.76\%$ ,  $V_f = 0.20$



(l) Dilated design,  $\Delta = 0.054$  mm  
 $M_{nd} = 0.39\%$ ,  $V_f = 0.22$

Fig. 7: The robust pressure-actuated gripper mechanisms. Filter radius  $5.4h$  is used for the optimized results displayed in rows 1 and 2, whereas for the results shown in rows 3 and 4 are obtained with filter radius  $8.4h$ . Note  $h = \min(\frac{L_x}{N_{ex}}, \frac{L_y}{N_{ey}})$ .

these would lead to disconnected structures in the eroded design with very poor performance, and hence the optimizer avoids such problematic features entirely. The topology for the dilated, intermediate and eroded is the same for all the presented cases. The eroded designs feature thin members, whereas the dilated designs consist of thicker branches, which is expected. Thicknesses of the members of the intermediate designs are between those

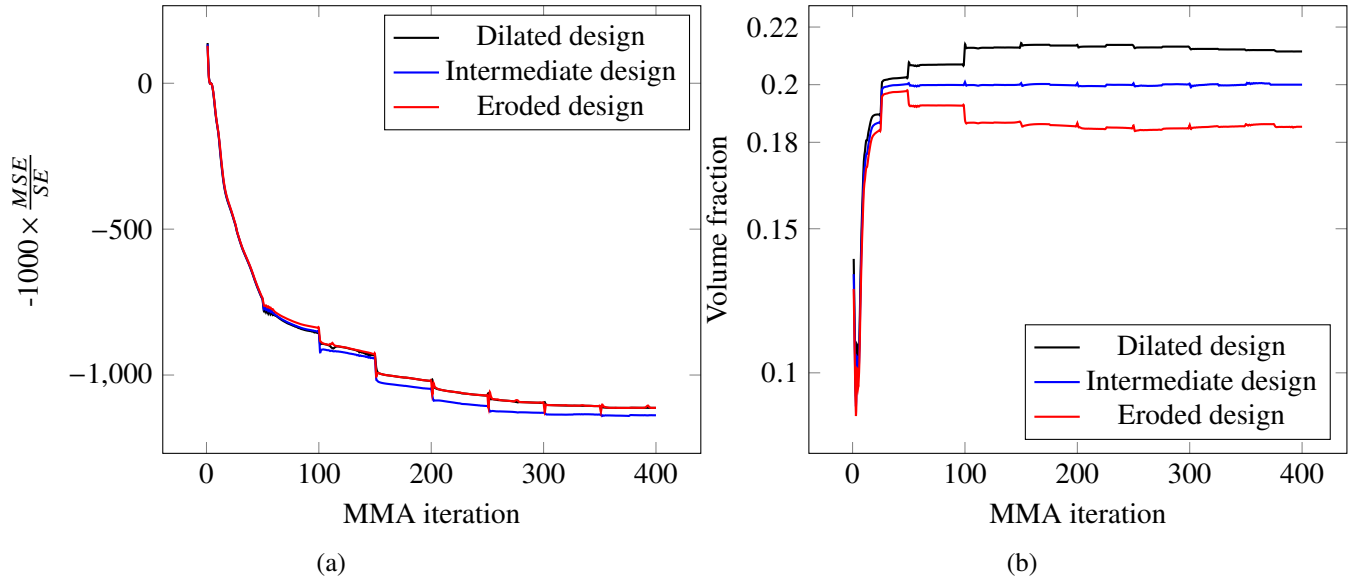


Fig. 8: Objective and volume fraction convergence plots for inverter CMs displayed in the first row of Fig. 6. (a) Objective history, and (b) Volume fraction history

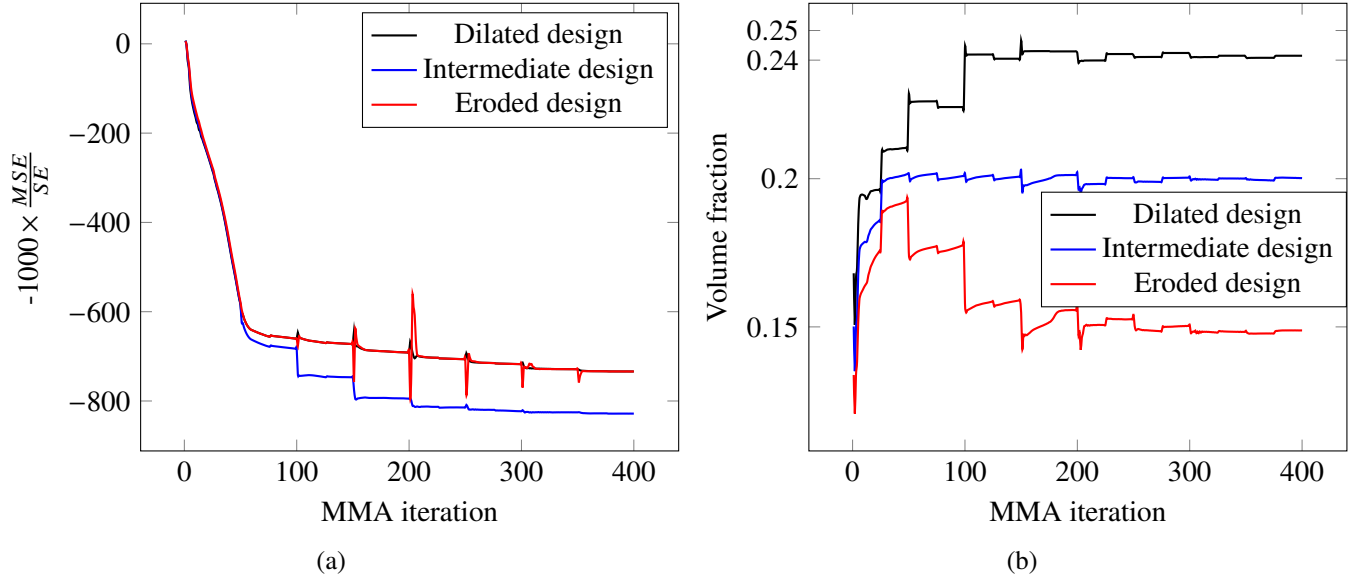


Fig. 9: Objective and volume fraction convergence plots for gripper CMs displayed in the third row of Fig. 6. (a) Objective history, and (b) Volume fraction history

of the respective eroded and dilated designs.  $M_{nd}$  and final volume fraction for each optimized design are also mentioned. The obtained solutions in Fig. 6 and Fig. 7 are very close to 0-1 designs as their  $M_{nd}$  values are low. This is a very desirable result, since now the design interpretation no longer significantly changes the geometry of the design and its performance. In all cases, the final volume fractions of the optimized intermediate designs are observed to be equal to the permitted volume fraction, i.e., 0.20. It is noticed that the optimized mechanisms obtained with  $\Delta\eta = 0.15$  have larger minimum length scale than those obtained with  $\Delta\eta = 0.05$  at the same filter radius. In addition, the optimized mechanisms with same  $\Delta\eta$  but higher filter radius have larger minimum length scale. Therefore, the minimum feature size increases with increase in  $\Delta\eta$  and is also a function of the filter radius, which are known properties of the robust formulation [24].

The layout of the optimized inverter mechanisms is more or less same as their traditional counterparts. In case of the gripper mechanisms, we obtain designs having a large space for fluid to inflate. This is reminiscent of designs

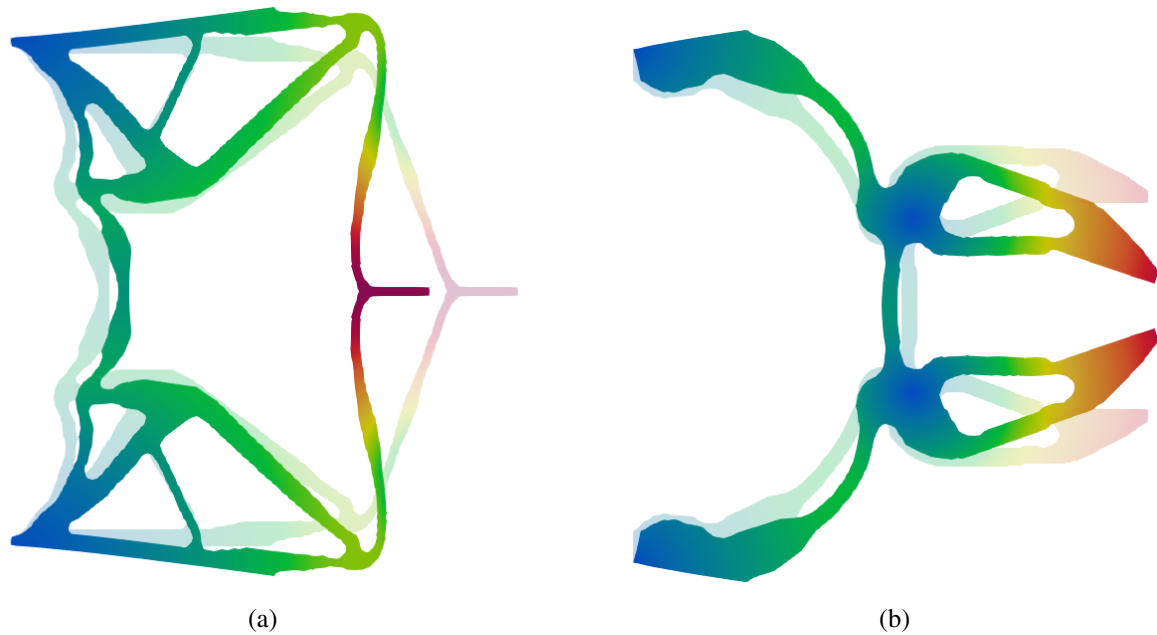


Fig. 10: Deformed profiles of the optimized inverter and gripper CMs are displayed with 50 times magnified displacement obtained from linear analysis. Red and blue indicate the maximum and minimum displacements, respectively.

of pneumatically-actuated soft robots. The obtained output deformations of the optimized eroded mechanisms are higher than the intermediate designs in each case (Fig. 6 and Fig. 7), however, as mentioned before, such designs have lower manufacturing limits and as-fabricated designs may be fragile. Figures 8 and 9 indicate the convergence history of the objective and volume constraints for the optimized inverter mechanisms depicted in the first row of Fig. 6 and the optimized gripper CMs displayed in the third row of Fig. 7, respectively. One notices a smooth convergence, and the volume constraint is active for the intermediate design at the end of the optimization for both the mechanisms (Figs. 8 and 9). The objective values of the intermediate designs are lower than those of the corresponding eroded and dilated designs (Figs. 8 and 9), indicating that intermediate designs are the best performing ones in the view of the considered multi-criteria objective that determines a balance between the output displacement and strength of the mechanism. The objectives of respective eroded and dilated designs are close to each other at the end of the optimization (Figs. 8 and 9). The deformed profiles for the full intermediate inverter and gripper mechanisms at 50 times magnified linear deformation are displayed in Fig. 10a and Fig. 10b, respectively. These P-CMs perform as expected, however the deformation profiles are far from those obtained when using nonlinear mechanics with high pressure loads, as studied next.

### 4.3 Large deformation analyses

In this section, the optimized compliant mechanisms are tested with high pressure loadings to investigate their behaviors under large deformation cases. In the FE analysis, geometric nonlinearity will now be considered. In addition, instead of the linear material model, a neo-Hookean material model with the following strain energy function  $W$  [16] is employed

$$W = \frac{G}{2} [\text{tr}(\mathbf{F}\mathbf{F}^T) - 3 - 2\ln J] + \frac{\lambda}{2} (\ln J)^2, \quad (20)$$

where  $\mathbf{F} = \nabla_0 \mathbf{u} + \mathbf{I}$  is the deformation gradient and  $G = \frac{E_1}{2(1+\nu)}$  and  $\lambda = \frac{2G\nu}{1-2\nu}$  are Lamé's constants.  $\nabla_0 \mathbf{u}$  denotes gradient of the displacement field  $\mathbf{u}$  with respect to reference coordinates  $\mathbf{X}$ , and  $\nu$  is Poisson's ratio.  $J = \det(\mathbf{F})$ , and  $\mathbf{I}$  is the unit tensor. Typically, rubber-like materials are used for pneumatically-actuated mechanisms [36] and

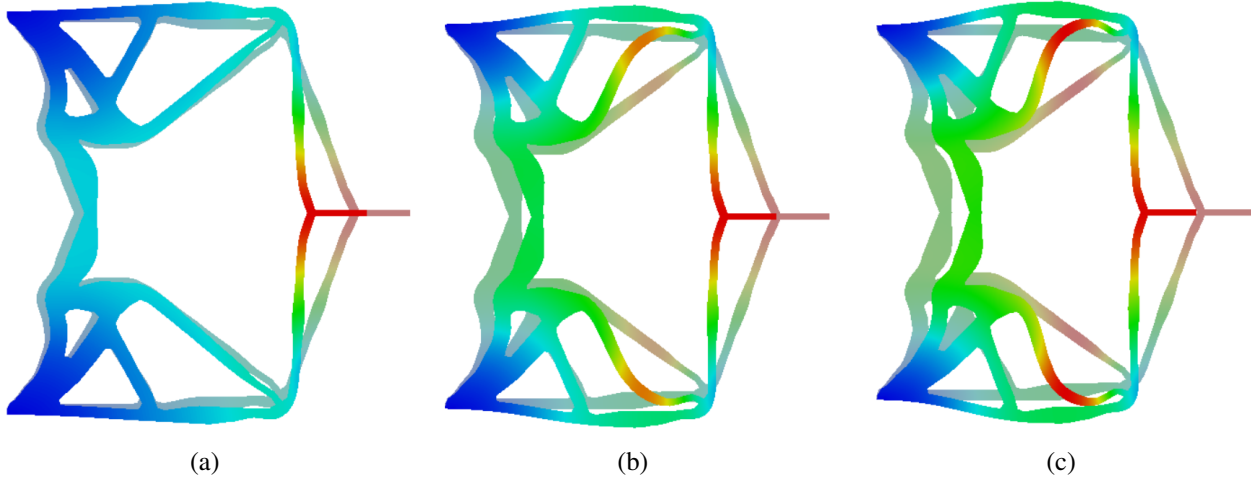


Fig. 11: Deformed profiles of the inverter CM at different pressure loads. (a) 50 bar, (b) 100 bar, and (c) 150 bar. At 150 bar pressure loading, branches of the inverter mechanism come in contact with each other. Blue and red color indicate minimum and maximum deformation locations, respectively.

to numerically model such materials, a neo-Hookean material description can be employed [16].

Using the fundamentals of the continuum mechanics, the Cauchy stress tensor  $\sigma$  can be determined from the strain energy function noted in Eq. 20 as

$$\sigma = \frac{G}{J}(\mathbf{F}\mathbf{F}^T - \mathbf{I}) + \frac{\Lambda}{J}(\ln J)\mathbf{I}. \quad (21)$$

Following the nonlinear FE formulation, the displacement vector  $\mathbf{u}$  is determined by solving

$$\mathbf{R}(\mathbf{u}) = \mathbf{F}_{\text{int}}(\mathbf{u}) - \mathbf{F}_{\text{ext}}(\mathbf{u}) = \mathbf{0}, \quad (22)$$

where  $\mathbf{R}(\mathbf{u})$  is the residual force and  $\mathbf{F}_{\text{ext}}(\mathbf{u})$  is the external force arises due to the pressure loading. The internal force vector  $\mathbf{F}_{\text{int}}^e(\mathbf{u})$  at the element level is determined as

$$\mathbf{F}_{\text{int}}^e = \int_{\Omega^e} \mathbf{B}_{\text{UL}}^T(\mathbf{u})\sigma_e(\mathbf{u}) d\Omega^e, \quad (23)$$

where  $\mathbf{B}_{\text{UL}}(\mathbf{u})$  and  $\sigma_e$  are the updated Lagrangian strain-displacement matrix and the Cauchy stress tensor of an FE  $\Omega^e$ , respectively. Eq. 22 can be solved using a Newton-Raphson (N-R) iterative process. Note also that,  $\mathbf{F}_{\text{ext}}(\mathbf{u})$  varies as it arises from pressure loading which follows the surface where it is applied upon, i.e., it is a follower force and thus, contributes in the tangent stiffness of the nonlinear equations. Herein, we use ABAQUS for the nonlinear finite element analyses.

The intermediate optimized designs of the inverter and gripper mechanisms displayed in the first row of Fig. 6 and third row of Fig. 7 are selected for the nonlinear analyses in ABAQUS. First, the boundaries of the optimized designs are extracted, and corresponding 2D CAD models are generated. Thereafter, using these CAD models, nonlinear FE analyses while considering follower force characteristics of the pressure loads are performed with input pressure 50 bar, 100 bar and 150 bar in ABAQUS. Figure 11 and Fig. 12 display the deformed profiles of the CMs with high pressure loadings. As pressure loads increase the deformation of the P-CMs also increase, which is expected and natural. At 150 bar, inverter mechanisms experience self-contact (Fig. 11c) that indicates that one may have to include self-contact conditions [27] between the branches of the mechanisms when dealing



with high pressure loadings for the large deformation cases. For the inverter mechanisms, the deformation profiles in Fig. 10a and Fig. 11a are different, and the output displacement has reduced by 78 %. Likewise, the deformed continua in Fig. 10b and Fig. 12a are not the same. Although the gripper still exhibits the intended functionality, the magnitude of the jaw displacement has reduced by 82 %. Figure 13 shows the output displacements obtained with the linear and nonlinear analyses at different pressure loads for the inverter and gripper mechanisms. The displacements obtained with linear analyses are far from the full nonlinear analyses for both the mechanisms (Figs. 13a and 13b). These indicate limitations and shortcomings of the P-CMs obtained assuming linear elasticity concepts. Therefore, ideally, one has to include full nonlinear mechanics (with contact) within the design approach for high pressure loadings wherein P-CMs can experience large deformations and even self and/or mutual contact.

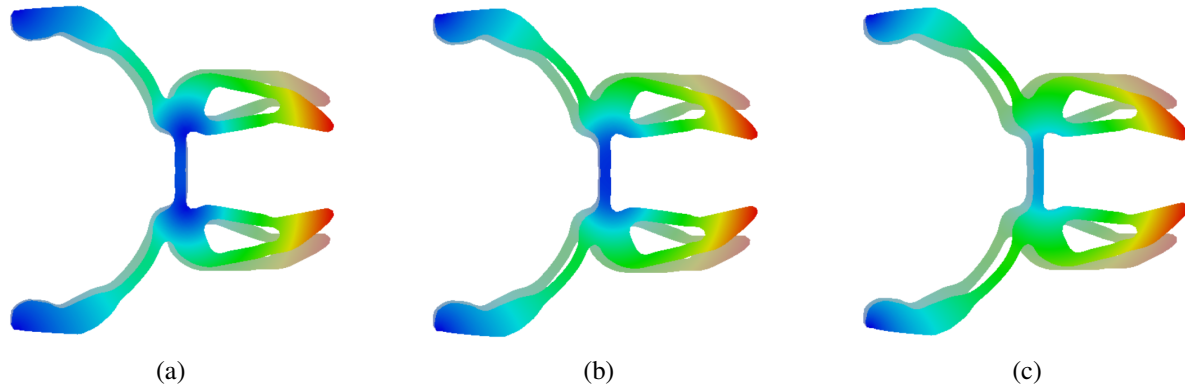


Fig. 12: Deformed profiles of the gripper CM at different pressure loads. (a) 50 bar, (b) 100 bar, and (c) 150 bar. Blue and red color indicate minimum and maximum deformation locations, respectively.

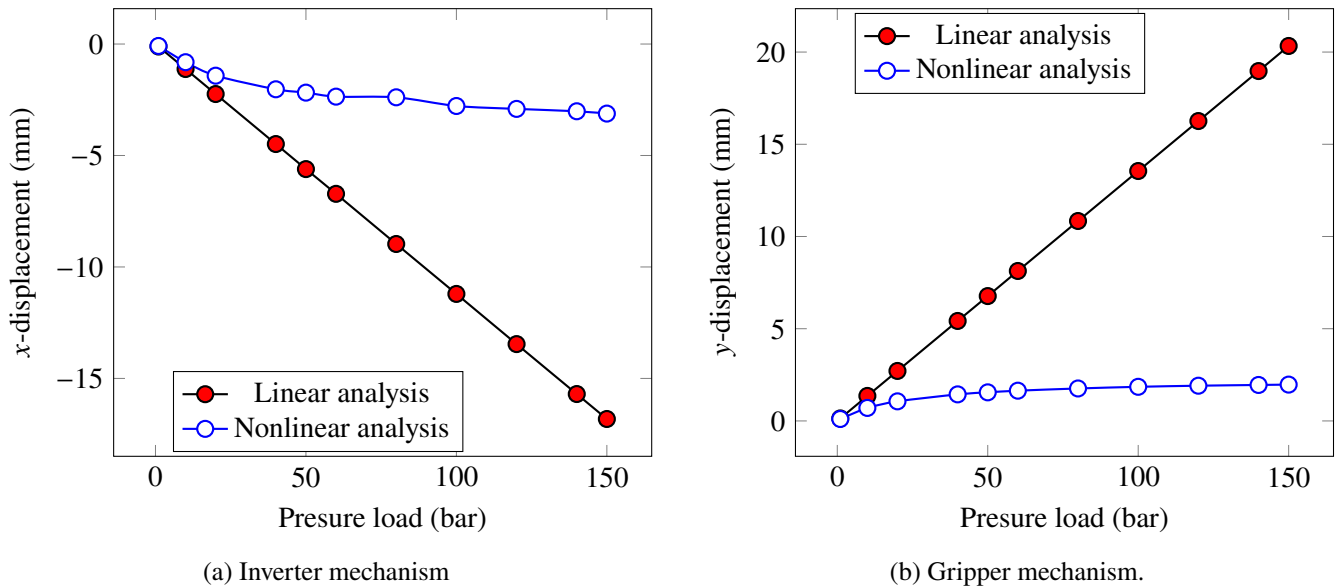


Fig. 13: The output displacements obtained from the linear and nonlinear analyses using different pressure loads. For the gripper mechanism, the displacements corresponding to the lower jaw are indicated.

## 5 Closure

With the aim to bridge the gap between optimized and as-fabricated designs, this paper presents a density-based topology optimization approach to generate pressure-actuated robust compliant mechanisms. The robust formulation, i.e., the eroded, intermediate (blueprint) and dilated projections for the design description is employed for the first time to this problem class, in combination with a representation of the pressure loads using the Darcy law in combination with a drainage term. Well-functioning pressure-actuated robust inverter and gripper mechanisms are obtained with different robustness levels and filter radii to illustrate different minimum length scales of the mechanisms. Single-node hinges, that cannot be fabricated but frequently appear when using the traditional topology optimization approach, are no longer found in the obtained designs. The approach solves three sets of equilibrium equations and uses a continuation approach for the projection parameter  $\beta$  that requires a large number of the optimization iterations and thus, computational cost increases. The approach provides three physical material density vectors with one design variable vector. Intermediate designs can be used for manufacturing purposes.

The obtained optimized designs are close to binary. This eliminates the loss of performance observed when grayscale topology optimization results are post-processed into CAD geometries for fabrication. The intermediate designs are used to study behavior of the mechanisms with high pressure loads while accounting for geometric and material nonlinearity. It is found that the scaled linear deformation profiles and those obtained with full nonlinear analyses do not match well. Moreover, at high pressures self-contact of mechanism branches occurs. These observations indicate that for further development of topology optimization for pressure-actuated compliant mechanisms, next to the robust formulation, considering nonlinear mechanics and self-contact may be indispensable.

## Acknowledgments

P. Kumar acknowledges financial support from the Science & Engineering research board, Department of Science and Technology, Government of India under the project file number RJF/2020/000023. The authors acknowledge Prof. Krister Svanberg for providing MATLAB codes of the MMA optimizer.

## References

- [1] M. Frecker, G. K. Ananthasuresh, S. Nishiwaki, N. Kikuchi, and S. Kota, "Topological synthesis of compliant mechanisms using multi-criteria optimization," *Journal of Mechanical design*, vol. 119, no. 2, pp. 238–245, 1997.
- [2] L. L. Howell, *Compliant Mechanisms*. John Wiley & Sons, New York, 2001.
- [3] P. Kumar, P. Fanzio, L. Sasso, and M. Langelaar, "Compliant fluidic control structures: Concept and synthesis approach," *Computers & Structures*, vol. 216, pp. 26–39, 2019.
- [4] P. Kumar, C. Schmidleithner, N. Larsen, and O. Sigmund, "Topology optimization and 3D printing of large deformation compliant mechanisms for straining biological tissues," *Structural and Multidisciplinary Optimization*, vol. 63, no. 3, pp. 1351–1366, 2021.
- [5] G. K. Ananthasuresh, "The art and signs of a few good mechanical designs in MEMS," in *Mechanical Sciences*, pp. 29–56, Springer, 2021.
- [6] B. Zhu, X. Zhang, H. Zhang, J. Liang, H. Zang, H. Li, and R. Wang, "Design of compliant mechanisms using continuum topology optimization: A review," *Mechanism and Machine Theory*, vol. 143, p. 103622, 2020.
- [7] O. Sigmund and K. Maute, "Topology optimization approaches," *Structural and Multidisciplinary Optimization*, vol. 48, no. 6, pp. 1031–1055, 2013.
- [8] P. Kumar, J. S. Frouws, and M. Langelaar, "Topology optimization of fluidic pressure-loaded structures and compliant mechanisms using the darcy method," *Structural and Multidisciplinary Optimization*, pp. 1–19, 2020.
- [9] F. Chen, W. Xu, H. Zhang, Y. Wang, J. Cao, M. Y. Wang, H. Ren, J. Zhu, and Y. Zhang, "Topology optimized design, fabrication, and characterization of a soft cable-driven gripper," *IEEE Robotics and Automation Letters*, vol. 3, no. 3, pp. 2463–2470, 2018.
- [10] Y. Luo, J. Xing, and Z. Kang, "Topology optimization using material-field series expansion and kriging-based algorithm: An effective non-gradient method," *Computer Methods in Applied Mechanics and Engineering*, vol. 364, p. 112966, 2020.
- [11] O. Sigmund, "On the design of compliant mechanisms using topology optimization," *Journal of Structural Mechanics*, vol. 25, no. 4, pp. 493–524, 1997.
- [12] L. Yin and G. K. Ananthasuresh, "Design of distributed compliant mechanisms," *Mechanics Based Design of Structures and Machines*, vol. 31, no. 2, pp. 151–179, 2003.
- [13] V. B. Hammer and N. Olhoff, "Topology optimization of continuum structures subjected to pressure loading," *Structural and Multidisciplinary Optimization*, vol. 19, no. 2, pp. 85–92, 2000.
- [14] B. C. Chen and N. Kikuchi, "Topology optimization with design-dependent loads," *Finite elements in analysis and design*, vol. 37, no. 1, pp. 57–70, 2001.
- [15] O. Sigmund and P. M. Clausen, "Topology optimization using a mixed formulation: An alternative way to solve pressure load problems," *Computer Methods in Applied Mechanics and Engineering*, vol. 196, no. 13–16, pp. 1874–1889, 2007.
- [16] O. C. Zienkiewicz and R. L. Taylor, *The Finite Element Method for Solid and Structural Mechanics*. Butterworth-Heinemann, 2005.
- [17] B. C. Chen, E. C. Silva, and N. Kikuchi, "Advances in computational design and optimization with application to mems," *International Journal for Numerical Methods in Engineering*, vol. 52, no. 1–2, pp. 23–62, 2001.
- [18] H. Paganiban, G. W. Jang, and T. J. Chung, "Topology optimization of pressure-actuated compliant mechanisms," *Finite Elements in Analysis and Design*, vol. 46, no. 3, pp. 238–246, 2010.
- [19] S. Vasista and L. Tong, "Design and testing of pressurized cellular planar morphing structures," *AIAA journal*, vol. 50, no. 6, pp. 1328–1338, 2012.

- [20] E. M. de Souza and E. C. N. Silva, "Topology optimization applied to the design of actuators driven by pressure loads," *Structural and Multidisciplinary Optimization*, pp. 1–24, 2020.
- [21] P. Kumar and M. Langelaar, "On topology optimization of design-dependent pressure-loaded three-dimensional structures and compliant mechanisms," *International Journal for Numerical Methods in Engineering*, vol. 122, no. 9, pp. 2205–2220, 2021.
- [22] T. A. Poulsen, "A new scheme for imposing a minimum length scale in topology optimization," *International Journal for Numerical Methods in Engineering*, vol. 57, no. 6, pp. 741–760, 2003.
- [23] R. Saxena and A. Saxena, "On honeycomb representation and sigmoid material assignment in optimal topology synthesis of compliant mechanisms," *Finite Elements in Analysis and Design*, vol. 43, no. 14, pp. 1082–1098, 2007.
- [24] F. Wang, B. S. Lazarov, and O. Sigmund, "On projection methods, convergence and robust formulations in topology optimization," *Structural and Multidisciplinary Optimization*, vol. 43, no. 6, pp. 767–784, 2011.
- [25] P. Kumar, A. Saxena, and R. A. Sauer, "Implementation of self contact in path generating compliant mechanisms," in *Microactuators and Micromechanisms*, pp. 251–261, Springer, 2017.
- [26] P. Kumar, R. A. Sauer, and A. Saxena, "Synthesis of  $C^0$  path-generating contact-aided compliant mechanisms using the material mask overlay method," *Journal of Mechanical Design*, vol. 138, no. 6, p. 062301, 2016.
- [27] P. Kumar, A. Saxena, and R. A. Sauer, "Computational synthesis of large deformation compliant mechanisms undergoing self and mutual contact," *Journal of Mechanical Design*, vol. 141, no. 1, p. 012302, 2019.
- [28] N. P. van Dijk, M. Langelaar, and F. van Keulen, "Element deformation scaling for robust geometrically nonlinear analyses in topology optimization," *Structural and Multidisciplinary Optimization*, vol. 50, no. 4, pp. 537–560, 2014.
- [29] B. S. Lazarov, F. Wang, and O. Sigmund, "Length scale and manufacturability in density-based topology optimization," *Archive of Applied Mechanics*, vol. 86, no. 1-2, pp. 189–218, 2016.
- [30] T. E. Bruns and D. A. Tortorelli, "Topology optimization of non-linear elastic structures and compliant mechanisms," *Computer Methods in Applied Mechanics and Engineering*, vol. 190, no. 26, pp. 3443–3459, 2001.
- [31] J. K. Guest, J. Prévost, and T. Belytschko, "Achieving minimum length scale in topology optimization using nodal design variables and projection functions," *International Journal for Numerical Methods in Engineering*, vol. 61, no. 2, pp. 238–254, 2004.
- [32] O. Sigmund, "Morphology-based black and white filters for topology optimization," *Structural and Multidisciplinary Optimization*, vol. 33, no. 4-5, pp. 401–424, 2007.
- [33] D. Trillet, P. Duysinx, and E. Fernández, "Analytical relationships for imposing minimum length scale in the robust topology optimization formulation," *arXiv preprint arXiv:2101.08605*, 2021.
- [34] A. Saxena and G. K. Ananthasuresh, "On an optimal property of compliant topologies," *Structural and multidisciplinary optimization*, vol. 19, no. 1, pp. 36–49, 2000.
- [35] K. Svanberg, "The method of moving asymptotes—a new method for structural optimization," *International Journal for Numerical Methods in Engineering*, vol. 24, no. 2, pp. 359–373, 1987.
- [36] F. Schmitt, O. Piccin, L. Barbé, and B. Bayle, "Soft robots manufacturing: A review," *Frontiers in Robotics and AI*, vol. 5, p. 84, 2018.